

2-Shots in the Dark: Low-Light Denoising with Minimal Data Acquisition

Liying Lu

Raphaël Achddou

Sabine Süsstrunk

IVRL, EPFL

liying.lu@epfl.ch

raphael.achddou@esiee.fr

sabine.susstrunk@epfl.ch

Abstract

Raw images taken in low-light conditions are very noisy due to low photon count and sensor noise. Learning-based denoisers have the potential to reconstruct high-quality images. For training, however, these denoisers require large paired datasets of clean and noisy images, which are difficult to collect. Noise synthesis is an alternative to large-scale data acquisition: given a clean image, we can synthesize a realistic noisy counterpart. In this work, we propose a general and practical noise synthesis method that requires only **one single noisy image and one single dark frame** per ISO setting. We represent signal-dependent noise with a Poisson distribution and introduce a Fourier-domain spectral sampling algorithm to accurately model signal-independent noise. The latter generates diverse noise realizations that maintain the spatial and statistical properties of real sensor noise. As opposed to competing approaches, our method neither relies on simplified parametric models nor on large sets of clean-noisy image pairs. Our synthesis method is not only accurate and practical, it also leads to state-of-the-art performances on multiple low-light denoising benchmarks.

1 Introduction

Capturing images in low-light conditions with consumer cameras often results in extremely noisy photographs. To restore clean images from noisy ones, numerous denoising techniques have been developed, including deep learning-based methods [5, 9, 28, 30, 39, 42]. For such models, the quality of training data is crucial, as it largely determines model effectiveness. Consequently, acquiring appropriate training data is a central challenge.

A common approach is to collect large datasets consisting of clean-noisy image pairs [1, 3, 9, 13]. Each pair is obtained by capturing the same scene with different camera settings using a tripod and remote control to obtain well-aligned pairs. This cumbersome process is repeated for multiple scenes.

Noise synthesis has therefore become an active research area, as it allows bypassing the acquisition of such large datasets. However, this task is harder than it appears. While the assumption of Additive White Gaussian Noise (AWGN) has been used in the vast majority of the image denoising literature [6, 18, 42–44], this model fails to replicate the complex nature of real-world camera noise, resulting in poor performance for denoisers trained under this assumption.

In practice, sensor noise is the sum of multiple noise sources, which can be divided into signal-dependent and signal-independent components. While signal-dependent noise mainly consists of photon shot noise, signal-independent noise is far more complex and difficult to model.

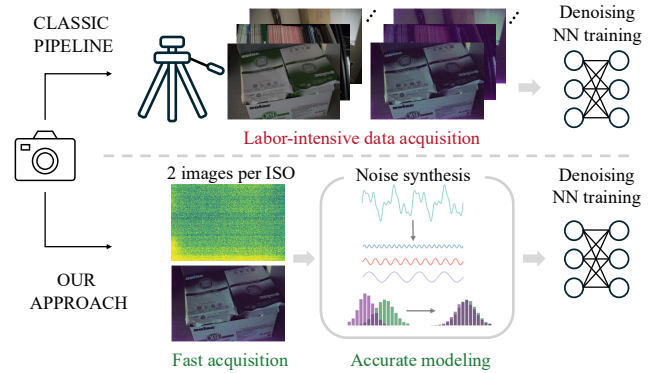


Figure 1: Different from classic denoising pipelines that require large amounts of paired data, we propose a precise sensor noise synthesis method that requires only a single noisy image and a single dark frame. From these two inputs, our algorithm accurately reproduces the sensor noise distribution without the need for complex parameter calibration.

It includes dark current noise [25], thermal noise [17], reset noise [10, 25], and banding pattern noise [10, 17, 38].

Prior methods [10, 38] modeled these noise sources with simple parametric models. These methods face two critical limitations: their lack of expressivity and the need for careful parameter calibration. Another direction consists of learning the noise distribution using neural networks, including GANs [32, 40], normalizing flows [2], and diffusion

models [29]. These approaches have demonstrated significant improvements but still rely on large amounts of paired clean-noisy data for learning the noise distribution.

In this paper, we propose an accurate sensor noise synthesis method that requires only *a single noisy image and a single dark frame*, with the latter captured in a lightless environment. From these two inputs, our algorithm reproduces the sensor noise distribution without the need for complex parameter tuning, significantly reducing the time and effort required for data acquisition and calibration.

Similar to prior works [12, 38, 45], we model signal-dependent noise with a Poisson distribution, whose parameters can be estimated from the noisy image via straightforward linear regression. Our main contribution lies in the modeling of signal-independent noise. We introduce a Fourier-domain spectral sampling method that is both practical and general. Given a single dark frame, we compute its Fourier transform and apply phase randomization while preserving the magnitude spectrum. This process generates novel noise realizations that maintain the spectral characteristics of the original sensor noise. Meanwhile, histogram matching is employed to ensure that the marginal distribution of the synthetic noise aligns with the real noise.

Our method provides three key advantages for signal-independent noise modeling: (1) It is a unified framework for modeling all signal-independent noise components; no labor-intensive calibration or acquisition is needed. (2) It is a general solution applicable to different types of sensors. (3) Generated noise preserves both the spectral characteristics and marginal distribution of real sensor noise, ensuring a realistic synthesis.

Overall, the proposed method provides an accurate and practical solution with minimal data acquisition for sensor noise synthesis, enabling the generation of unlimited clean-noisy pairs for training image denoising models. Our experiments show that denoising networks trained with our synthetic data are on par with the state-of-the-art models.

2 Related Work

2.1 Physics-Based Noise Modeling

A more realistic alternative to the AWGN approximation of noise used in the vast majority of the denoising literature is the Poisson–Gaussian (PG) model [4, 5, 14, 15]. This model decomposes noise into two components: a signal-dependent Poisson noise arising from the stochastic nature of photon capture, and a signal-independent Gaussian noise approximating sensor readout noise.

While this model captures fundamental aspects of sensor noise, it does not fully represent the diversity of noise sources encountered in practice. More sophisticated models [10, 14, 37, 38, 41] were therefore proposed to incorporate additional noise sources. For instance, the ELD [38]

Table 1: Summary of typical learning-based and non-learning-based noise synthesis methods, along with the number of real image pairs and dark frames used for data synthesis on the SID dataset [9].

Method	Category	# of real pairs	# of dark frames (per ISO)
LRD [40]	Learning	1865	400 ¹
NoiseDiff [29]	Learning	1865	400 ²
PMN [12]	Non-learning	1865	400
ELD [38]	Non-learning	0	Several ³
SFRN [45]	Non-learning	0	10
Ours	Non-learning	0	1
Poisson-Gaussian	Non-learning	0	0

paper models the read noise with a Tukey-Lambda distribution [22] to better account for its long-tailed profile and color-biases. Other noise components, such as banding noise, are also considered. ELD estimates noise parameters using flat-field frames and dark frames. *Flat-field frames* are photographs of a white sheet placed against a uniformly illuminated wall, whereas *dark frames* are captured in a dark room with the camera lens capped. Despite the more precise noise modeling, the approach remains oversimplified and requires labor-intensive multi-parameter calibration. The SFRN paper [45] proposes to synthesize noise by directly sampling real dark frames from the sensor. It models signal-dependent noise using a Poisson distribution, and samples patches from a dark-frame database containing 10 dark frames per ISO setting to mimic signal independent noise. Our approach shares some similarities with theirs, as we also treat signal-dependent and signal-independent noise separately, and the latter is sampled from a real dark frame exemplar. However, there are key differences. Since they crop patches from a small set of dark frames for modeling signal dependent noise, the diversity of the noise samples is somewhat limited. In contrast, our spectral sampling method enables the generation of a much more diverse set of noise samples, starting from a single exemplar.

PMN [12] proposes applying shot noise augmentation to real clean-noisy pairs. It introduces a *dark shading correction* scheme, where hundreds of dark frames are averaged per ISO and linear regression is applied to estimate a combination of black level error (BLE) [33] and fixed-pattern noise (FPN) [7, 21]. Subtracting this estimated dark shading from noisy images simplifies subsequent denoising.

2.2 Deep Learning-Based Noise Modeling

Recent studies have explored modeling noise distributions through data-driven approaches based on deep neural networks. Noise Flow [2] trains a normalizing flow [11, 23, 24]

¹LRD uses the dark shadings from PMN.

²NoiseDiff uses the dark shadings from PMN.

³Not mentioned in the ELD paper, but the number is more than one.

to model noise in the RAW domain, and Kousha *et al.* [26] extend flow-based modeling to the sRGB space. LLD [8] proposes to learn different noise components by different normalizing flow layers. LRD [40] combines a Poisson model for signal-dependent noise with a GAN for learning signal-independent components. Monakhova *et al.* [32] propose a noise generator that learns the parameters of a physics-based model, eliminating manual calibration. NoiseDiff [29] introduces a diffusion model to learn the sensor noise distribution and achieves superior results. Despite significant progress, these learning-based methods still face several challenges. Normalizing Flow models lack expressiveness for modeling complex distributions because of architectural constraints. GANs are prone to training instability [19, 31]. Diffusion models [34, 35] provide more accurate noise modeling but suffer from a relatively slow generation speed. Moreover, all these models still require a certain amount of real paired data for training. In contrast, our method does not rely on any paired data. It requires only a single noisy image and one dark frame, yet it can generate infinitely diverse samples with high efficiency. We summarize the amount of data used by different synthesis methods for noise generation in Table 1.

3 Method

3.1 Spectral Sampling for Dark Frame Synthesis

We aim to model the complex signal-independent noise, which includes multiple components such as fixed-pattern noise (FPN), dark current shot noise, read noise, and banding pattern noise. Parametric models require laborious sensor-specific calibration, yet still struggle to capture the full complexity of real noise.

We reinterpret this problem from a *texture synthesis* perspective, drawing inspiration from the random phase noise (RPN) algorithm [16, 27, 36]. The RPN algorithm synthesizes textures by preserving the Fourier magnitude spectrum while randomizing the phase. For stationary stochastic textures, the magnitude encodes spatial correlations and frequency content, while the phase primarily determines spatial localization.

Interestingly, signal-independent noise in dark frames exhibits approximately stationary properties after removal of the fixed-pattern noise. This property makes Fourier-domain synthesis particularly suitable for modeling sensor noise: by preserving the magnitude spectrum from a reference dark frame and randomizing its phase, we can generate new noise realizations that retain the frequency characteristics without requiring explicit parametric modeling.

Furthermore, we incorporate iterative histogram matching to ensure that the synthesized noise matches both the spectral characteristics and the full marginal distribution of the reference noise, producing noise realizations that closely reflect

real sensor properties. The entire pipeline is illustrated in Fig. 2.

3.1.1 Fixed-Pattern Removal

Dark frames contain both *structured* low-frequency patterns (e.g., bias shading, fixed-pattern noise) and *stochastic* signal-independent noise. Direct spectral analysis of the dark frame would be dominated by these low-frequency components, biasing the estimated spectral statistics. To isolate the stochastic component, we estimate the fixed-pattern structure by applying a large-kernel Gaussian blur to the reference dark frame I_{dark} :

$$S = \mathcal{G}_\sigma * I_{\text{dark}}, \quad (1)$$

where \mathcal{G}_σ is a Gaussian kernel of standard deviation σ . This filtering isolates spatially smooth patterns and removes high-frequency variations. Subtracting this estimate yields the residual:

$$R' = I_{\text{dark}} - S, \quad (2)$$

which primarily contains the stochastic noise components. To focus on the noise fluctuations and simplify spectral analysis, we further remove the channel-wise mean:

$$\mu^R = \mathbb{E}[R'], R = R' - \mu^R, \quad (3)$$

where $\mathbb{E}[\cdot]$ is the channel-wise spatial averaging operator.

3.1.2 Spectral Prior Estimation

We then compute the 2D discrete Fourier transform (DFT) of the zero-mean noise residual R :

$$\hat{R} = \mathcal{F}\{R\}, \quad (4)$$

where $\mathcal{F}\{\cdot\}$ denotes the DFT applied independently to each color channel. The magnitude spectrum $|\hat{R}|$ encodes the characteristic frequency content and spatial correlation patterns of the sensor noise, serving as a *spectral prior* for subsequent synthesis.

3.1.3 Phase Randomization

To synthesize new noise realizations that preserve the magnitude spectrum of real signal-independent noise, we employ a phase randomization algorithm inspired by RPN. Starting from the magnitude spectrum $|\hat{R}|$ obtained from the reference residual noise, we introduce randomness by incrementing the phase with a random offset $\xi \in \mathbb{R}^{C \times H \times W}$.

ξ is obtained by first creating a single channel map ξ^0 sampled from a uniform distribution over $[-\pi, \pi]$, and replicating it across all color channels. Given ξ , we construct a new randomized spectrum \hat{N} :

$$\xi^0 \sim \mathcal{U}([-\pi, \pi]^{(H,W)}), \quad (5)$$

$$\xi = \text{replicate}(\xi^0, C), \quad (6)$$

$$\hat{N} = |\hat{R}| \odot \exp(i(\theta_{\hat{R}} + \xi)), \quad (7)$$

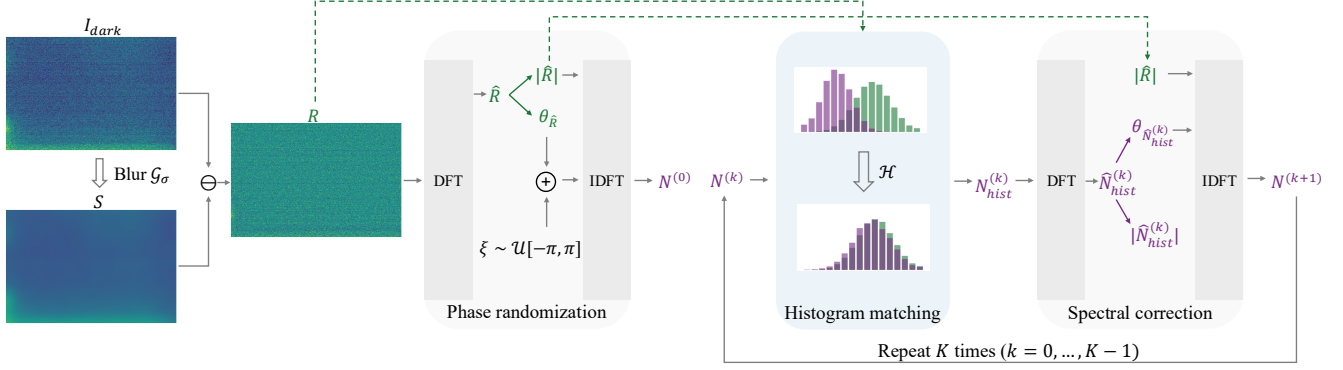


Figure 2: Overview of the spectral sampling algorithm. A Gaussian blur is applied to the real dark frame I_{dark} to estimate the fixed-pattern component S , which is then subtracted to obtain the stochastic residual R . In the Fourier domain, we retain the magnitude $|\hat{R}|$ and perform phase randomization using a uniform random phase ξ to obtain a new noise realization $N^{(0)}$. Subsequently, K iterations of histogram matching and spectral correction are applied to preserve both the marginal distribution and the spectral characteristics of the noise.

where $\theta_{\hat{R}}$ denotes the phase of \hat{R} , and \odot represents element-wise multiplication. This operation preserves the magnitude spectrum $|\hat{R}|$ while randomizing the phase to generate diverse noise instances.

A subtle but critical design choice is to replicate the same values across all channels of the phase offset ξ . In real sensor data, certain noise components such as banding patterns exhibit strong *inter-channel correlation*. Ensuring all channels share an identical random phase preserves these correlations. In contrast, applying independent phase offsets per channel would break them, producing unrealistic noise and leading to residual artifacts in images processed by denoisers trained on such synthetic data, as discussed in Section 4.5.

3.1.4 Inverse Transform and Initial Reconstruction

The synthesized noise realization is obtained by applying the inverse Fourier transform with proper normalization:

$$N^{(0)} = \frac{1}{\sqrt{HW}} \mathcal{F}^{-1}\{\hat{N}\}, \quad (8)$$

where H and W are the height and width of \hat{N} .

Although phase randomization preserves channel correlations and the magnitude spectrum, it does not guarantee the preservation of the reference noise histogram. Real sensor noise often exhibits non-Gaussian characteristics, including asymmetry and heavy tails [38], which the magnitude spectrum alone cannot capture. Ignoring these properties can lead to synthesized noise that appears visually plausible but does not accurately reproduce important noise statistics, such as mean, variance, skewness, and kurtosis, all of which are essential for training robust denoising models, as we demonstrate in Section 4.5.

3.1.5 Iterative Histogram and Spectral Refinement

To address this limitation, we introduce an iterative refinement procedure that alternates between histogram matching and spectral constraint enforcement. This approach ensures that the synthesized noise simultaneously satisfies both the spectral characteristics and the complete pixel-wise marginal distribution of the reference noise.

The refinement proceeds as follows. At iteration k , we first apply histogram matching to align the marginal distribution of $N^{(k)}$ with that of the reference residual R :

$$N'^{(k)}_{\text{hist}} = \mathcal{H}(N^{(k)}, R), \quad (9)$$

where $\mathcal{H}(\cdot, \cdot)$ denotes the histogram matching operator.

However, histogram matching may distort the frequency content and channel correlations. To restore these properties, we re-impose the spectral constraint:

$$N_{\text{hist}}^{(k)} = N'^{(k)}_{\text{hist}} - \mu_{\text{hist}}^{(k)}, \quad (10)$$

$$\hat{N}_{\text{hist}}^{(k)} = \mathcal{F}\{N_{\text{hist}}^{(k)}\}, \quad (11)$$

$$\hat{N}_{\text{corrected}}^{(k)} = |\hat{R}| \odot \exp(i\theta_{\hat{N}_{\text{hist}}^{(k)}}), \quad (12)$$

$$N^{(k+1)} = \frac{1}{\sqrt{HW}} \mathcal{F}^{-1}\{\hat{N}_{\text{corrected}}^{(k)}\} + \mu_{\text{hist}}^{(k)}, \quad (13)$$

where $\mu_{\text{hist}}^{(k)}$ is computed in a similar way to μ^R in Eq. 3. By preserving the phase from the histogram-matched sample while enforcing the reference magnitude spectrum, we maintain spatial randomness while restoring the correct spectral characteristics. To summarize, this iterative process alternates between two complementary constraints:

- **Histogram matching** ensures that the pixel-wise marginal distribution matches the reference.

- **Spectral correction** ensures that the frequency characteristics and spatial patterns match the reference.

3.1.6 Final Reconstruction

After K iterations, we reintroduce the deterministic low-frequency structure and channel means by adding back the fixed-pattern estimate S and the channel-wise mean μ^R :

$$\tilde{I}_{\text{dark}} = N^{(K)} + S + \mu^R. \quad (14)$$

This step ensures that the synthesized dark frames retain both the structured sensor biases and the realistic stochastic noise characteristics observed in real data.

We summarize the complete procedure in Algorithm 1 in the appendix.

3.2 Photon Noise Parameter Estimation

Photon noise can be approximated by the Poisson distribution because of the quantum nature of photons. To estimate the gain parameter g , we follow a similar approach as [12, 20, 38]. Generally, the noisy observation can be modeled as: $y = g\mathcal{P}(x) + n_{\text{other}}$, where x is the latent clean signal, \mathcal{P} denotes the Poisson distribution and n_{other} denotes signal-independent noise components. This would lead to a linear relationship between the variance of the noisy observation y and the amplified clean signal gx :

$$\text{Var}(y) = g(gx) + \text{Var}(n_{\text{other}}), \quad (15)$$

and a linear regression can be applied to estimate g . If only a single noisy image is available, a rough estimate of g can be obtained by first applying a Gaussian blur to approximate a pseudo clean image, and then using paired pixels from the noisy and pseudo clean images to fit the linear relationship. More details can be found in the appendix.

4 Experiments

4.1 Compared Methods

To assess the quality of the synthetic data, we compare the performance of denoising networks trained with data from different synthesis methods. We evaluate two recent learning-based methods (LRD [40] and NoiseDiff [29]), and four physics-based methods (the Poisson-Gaussian model, ELD [38], SFRN [45] and PMN [12])⁴. We also compare with a denoising network trained on real data pairs from the SID Sony training set. Among these methods, LRD, NoiseDiff and PMN still require large numbers of real clean-noisy pairs to synthesize new data. SFRN, ELD and our method synthesize data without the help of paired data.

⁴For LRD, NoiseDiff, ELD and PMN, we use pre-trained models available on the authors’ official websites. For SFRN, we use the reproduced code from the PMN repository whose results have been confirmed by the SFRN authors.

4.2 Implementation Details

For noise synthesis, we use images from the SID Sony training set [9], captured with a Sony A7S2 camera. We additionally use the dark-frame dataset from LLD [8], which contains 400 dark frames per ISO level, captured with the same camera model (though different physical devices). For each ISO level, we use one dark frame from the LLD dataset and one noisy image from the SID training set to synthesize dark frames. From these two images, we generate 400 synthetic dark frames for that ISO.

During denoising training, we take clean images from the SID training set and synthesize noisy images by applying Poisson noise and adding a randomly selected synthetic dark frame corresponding to the same ISO.

Among the compared methods, LRD, NoiseDiff, and PMN perform dark shading correction (DSC), where a pre-computed dark shading map is subtracted from the noisy inputs during both denoising training and inference (see Sec. 2.1). To ensure a fair comparison, we also train and test our denoiser with DSC. However, since we assume access to only a single dark frame per ISO, we estimate the dark shading map by applying Gaussian smoothing to that frame, as described in Sec. 3.1.1. More implementation details can be found in the appendix.

4.3 Image Denoising Performance Comparison

For denoising performance evaluation, we report results on the SID and ELD test sets. Table 2 reports the denoising performance of different methods. Although our approach synthesizes training data using only one noisy image and one dark frame per ISO, the denoising network trained on our synthetic data achieves strong performance across all exposure ratios on the SID and ELD test sets.

Among all methods, *NoiseDiff* achieves the best results on the SID dataset. However, it is a learning-based noise model that requires a large collection of clean-noisy pairs to learn the noise distribution (as shown in Table 1), and both its diffusion-based training and inference are computationally expensive. In contrast, among physics-based methods, our approach consistently achieves the best performance on the SID and ELD test sets across most exposure levels.

Figure 3 presents visual comparisons. In the first example from the SID test set, our method produces a cleaner reconstruction compared to other physics-based methods. In the second example from the ELD test set, our method effectively removes banding noise, whereas PG, ELD, and LRD leave noticeable residual banding. PMN also leaves visible noise in dark regions, and *NoiseDiff* introduces color deviations in the orange stripes.

4.4 Generalization to Different Sensors

To evaluate the generality of our approach, we further apply it to a different sensor using the LRID dataset [12], which is

Table 2: Denoising performance on the SID and ELD datasets in terms of PSNR / SSIM across various exposure ratios. Best results are in **bold**, and second-best results are underlined. *PG* denotes Poisson-Gaussian. *Real data* denotes the results obtained by using real paired data. *LRD* and *NoiseDiff* are learning-based methods, while others are non-learning-based methods. *LRD*, *NoiseDiff* and *PMN* require large numbers of real clean-noisy pairs to synthesize new data, while ours requires only one noisy image and one dark frame per ISO.

Dataset	Ratio	Real data	LRD [40]	NoiseDiff [29]	PG	ELD [38]	SFRN [45]	PMN [12]	Ours
SID	×100	42.95 / 0.958	43.16 / 0.958	43.92 / 0.961	41.05 / 0.936	41.95 / 0.953	42.81 / 0.957	43.47 / 0.961	<u>43.57 / 0.961</u>
	×250	40.27 / 0.943	40.69 / 0.941	41.28 / 0.946	36.63 / 0.885	39.44 / 0.931	40.18 / 0.934	41.04 / 0.947	41.24 / 0.945
	×300	37.32 / 0.928	37.48 / 0.919	37.90 / 0.929	33.34 / 0.811	36.36 / 0.911	37.09 / 0.918	<u>37.87 / 0.934</u>	<u>37.77 / 0.929</u>
ELD	×100	45.52 / 0.977	46.16 / 0.983	46.95 / 0.978	44.28 / 0.936	45.45 / 0.975	46.38 / 0.979	46.99 / 0.984	47.13 / 0.986
	×200	41.70 / 0.912	43.91 / 0.968	45.11 / 0.971	41.16 / 0.885	43.43 / 0.954	44.38 / 0.965	44.85 / <u>0.969</u>	<u>44.89 / 0.969</u>

Table 3: Denoising results on the LRID-Indoor (top) and -Outdoor (bottom) datasets in terms of PSNR / SSIM across various exposure ratios.

Ratio	Real data	PG	ELD [38]	SFRN [45]	PMN [12]	Ours
×64	48.80 / 0.991	46.98 / 0.988	48.26 / 0.990	48.18 / 0.990	<u>49.32 / 0.992</u>	49.47 / 0.992
×128	47.10 / 0.986	45.93 / 0.982	46.69 / 0.984	46.75 / 0.986	<u>47.60 / 0.987</u>	47.72 / 0.987
×256	44.89 / 0.979	44.09 / 0.970	44.47 / 0.974	44.84 / 0.979	<u>45.41 / 0.981</u>	45.50 / 0.979
×512	42.59 / 0.966	41.55 / 0.946	41.78 / 0.947	42.69 / 0.966	<u>43.14 / 0.967</u>	43.23 / 0.966
×1024	40.29 / 0.945	38.22 / 0.894	38.39 / 0.903	40.38 / 0.947	<u>40.67 / 0.948</u>	40.76 / 0.940
×64	45.85 / 0.988	42.51 / 0.980	45.09 / 0.984	45.18 / 0.985	<u>46.32 / 0.988</u>	46.31 / 0.988
×128	44.52 / 0.982	41.78 / 0.972	43.63 / 0.974	43.83 / 0.977	<u>44.90 / 0.983</u>	44.76 / 0.980
×256	42.71 / 0.971	40.59 / 0.953	41.52 / 0.948	42.08 / 0.961	<u>43.01 / 0.970</u>	42.72 / 0.958

captured with a Redmi K30 smartphone (IMX686 sensor). We follow the same data synthesis procedure as in the SID experiments, using one noisy image and one dark frame per ISO to synthesize noise.

Table 3 reports the quantitative results on the LRID test set. We primarily compare against state-of-the-art physics-based noise modeling methods. Our method consistently achieves superior performance on the LRID-Indoor test set and remains competitive on the LRID-Outdoor test set. While PMN attains higher performance on the LRID-Outdoor test set, it benefits from using hundreds of dark frames to estimate dark shading, which provides a strong prior and effectively stabilizes denoising training. Moreover, PMN still relies on a large number of real clean-noisy pairs for network training as shown in Table 1.

In contrast, our approach requires only a single noisy image and a single dark frame per ISO, yet achieves strong generalization across sensors without the need for extensive dark frame collections or clean-noisy datasets. This result suggests that our noise synthesis algorithm is scalable across various image sensors. Visual comparisons on the LRID dataset can be found in the appendix.

4.5 Discussions

Importance of inter-channel correlation. A critical but often overlooked aspect of sensor noise modeling is inter-channel correlation (ICC). Fig. 4 (first row) compares the ICC of real noise and noise synthesized with different methods. We compute Pearson correlation coefficients among

Table 4: Ablation study on inter-channel correlation (ICC) and iterative histogram matching (IHM). Results are reported in PSNR / SSIM on the SID and ELD test sets.

Dataset	Ratio	w/o ICC	w/o IHM	Ours
SID	×100	43.63 / 0.959	43.55 / 0.952	43.72 / 0.961
	×250	40.94 / 0.935	40.75 / 0.926	41.30 / 0.944
	×300	37.51 / 0.917	37.39 / 0.911	37.86 / 0.929
ELD	×100	47.18 / 0.986	47.06 / 0.984	47.14 / 0.986
	×200	44.82 / 0.967	44.81 / 0.966	44.78 / 0.966

the four color channels for each row, then average across all rows. Real noise shows clear positive correlations between some channels, while ELD [38] and our method without correlation enforcement produce nearly diagonal matrices, indicating spurious independence. Our full method reproduces correlations by using a shared random phase replicated across all channels (Eq. 5 and 6).

The reproduction of these correlations is crucial for training robust denoisers. The bottom row of Fig. 4 shows that denoisers trained with *ELD* or *Ours w/o ICC* data exhibit visible residual banding artifacts, while our method produces clean results. Table 4 reports the quantitative results. Removing ICC leads to consistently lower PSNR/SSIM on the SID dataset. The performance on the ELD dataset appears similar; however, as shown in the appendix, ICC remains crucial for suppressing banding noise.

Notably, our approach requires no explicit assumptions about channel or spatial correlations. By preserving the reference magnitude spectrum and controlling phase randomization, it naturally maintains the inherent correlation characteristics of each sensor.

Effect of iterative histogram matching. The iterative histogram matching (IHM) module is designed to align the marginal distribution of the synthesized noise with that of real noise. To analyze its effect, we compare synthesized noise with and without IHM. The first two columns of Fig. 5 show synthetic dark frames generated with and without IHM. Although their visual appearances are similar, the version without IHM exhibits a noticeable distribution mismatch

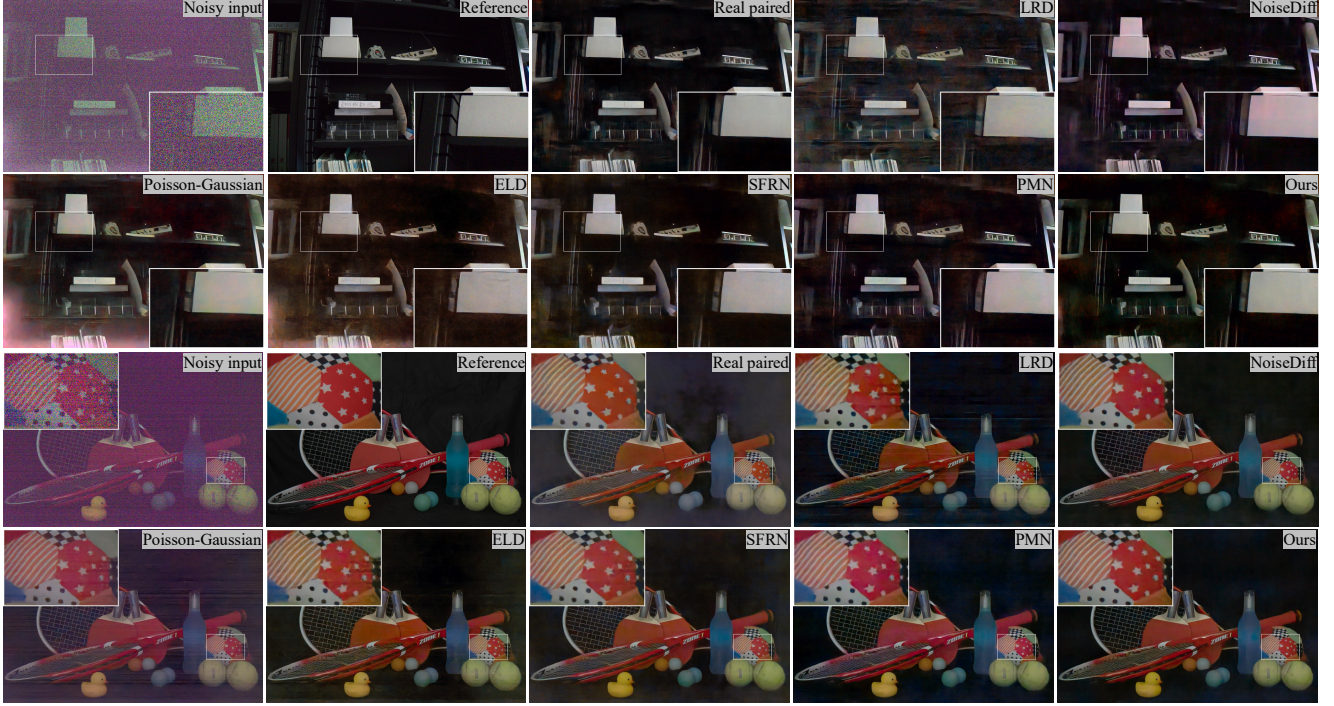


Figure 3: Result comparison of denoisers trained on data synthesized using different methods, along with a comparison to a denoiser trained on real pairs from the SID training set. The first example is from the SID test set, the second from the ELD test set. For both examples, our method produces cleaner results with fewer artifacts than other methods. Best viewed zoomed in. More results are provided in the appendix.

from real noise. Columns 4 and 5 of Fig. 5 show denoising results produced by networks trained on data synthesized with and without IHM. Without IHM, the reconstructed image exhibit color distortions, indicating that the distribution mismatch in the synthetic noise propagates to the downstream denoiser. With IHM, these artifacts are substantially reduced. We also observe that IHM helps suppress saturated malfunctioning pixels (see appendix), likely because it better preserves the long-tailed profile of the real noise histogram.

Finally, Table 4 summarizes the quantitative results. Removing IHM results in lower metrics, especially on the SID dataset. In all subsequent experiments, we set $K = 10$, as it provides a good balance between synthesis quality and computational cost.

Different ways to leverage a single dark frame. When only one real dark frame is available, several strategies can leverage it to generate paired training data, with additional Poisson noise applied to model signal-dependent noise: 1) *Direct addition*: Add the real dark frame to M clean images, producing M clean-noisy pairs, but all noisy samples share the same noise pattern. 2) *Patch-based sampling*: Crop random patches from the dark frame and add them to clean patches, as in SFRN [45], introducing some variation but limited diversity. 3) *Our method*: Generate multiple dark

frame variations, offering much greater diversity.

We perform an ablation study by training three denoisers on synthetic datasets generated by each method (*DirectAdd*, *RandomCrop*, *Ours*). Fig. 6 illustrates the denoising performance differences relative to the baseline *DirectAdd*. The purple lines show the Δ PSNR of *RandomCrop* minus the baseline, while the green lines show the Δ PSNR of *Ours* minus the baseline. A larger Δ indicates greater performance improvement over the baseline. Thus, random cropping provides a slight improvement, while our method noticeably improves performance, particularly at higher exposure ratios.

Realism validation of synthetic data. To further evaluate the realism of our synthetic noise, we train a denoising network using all available real dark frames. For a fair comparison, we generate synthetic dark frames with the same data volume and train another denoising network under identical settings. No performance degradation is observed, validating the realism of our synthetic data. Detailed experimental results are provided in the appendix.

Photon noise parameter estimation with limited data. As described in Sec. 3.2, the system gain g can be estimated using varying amounts of data. In our method, we assume only a single noisy image per ISO. In this ablation, we assess the effect of data availability by comparing denoising per-



Figure 4: Effect of inter-channel correlation (ICC). *First row*: Noise samples (ISO=50) from different methods, with row-wise averaged correlation matrices for Bayer channels (R, Gr, Gb, B). *Second row*: A clean-noisy pair and denoising results when denoisers are trained on different with different noise samplers. Real sensor noise exhibits cross-channel correlations, but ELD and our method without correlation enforcement produce nearly independent channels (near-diagonal matrices). Only our full method replicates the correlations. Consequently, denoisers trained with ELD or without correlation enforcement show residual banding artifacts, while our full method yields clean results.



Figure 5: Effect of iterative histogram matching (IHM). *Column 1-2*: synthetic noise without and with IHM (with histogram comparison and KLD to real noise). *Column 3*: a real clean-noisy pair. *Column 4-5*: the denoising results when training with data synthesized without and with IHM. Without IHM, there is a noticeable distribution misalignment between the **synthetic** and **real** noise, and the denoising result exhibits color artifacts. Whereas IHM improves noise realism and restoration quality. Best viewed zoomed in.

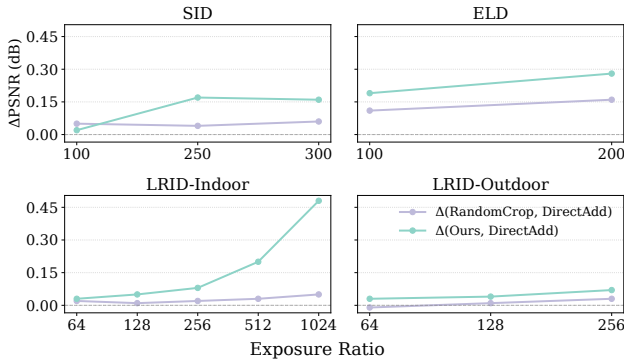


Figure 6: PSNR differences relative to the baseline *DirectAdd*: *RandomCrop* vs. *DirectAdd*, and *Ours* vs. *DirectAdd* across exposure ratios on the SID, ELD, and LRID test sets.

formance on the SID and ELD test sets when g is estimated using either one noisy image or 16 clean-noisy pairs. The experiment result (see appendix) shows that using a noisy image leads to a slight performance drop under some settings compared to using multiple clean-noisy pairs. For our main results (Table 2 and Table 3), we use the parameters estimated from a single noisy image per ISO. While in the above ablation studies, we use the parameters estimated from 16 clean-noisy pairs (fairness is ensured among all ablation studies).

5 Limitations and Conclusion

We addressed the challenge of obtaining large paired clean-noisy datasets for training low-light image denoisers by proposing a practical noise synthesis method that requires only one noisy image and one dark frame per ISO setting. We introduce a Fourier-domain spectral sampling strategy to model the complex signal-independent noise. This enables

the generation of diverse and physically accurate noise realizations that preserve both the spectral characteristics and the marginal statistics of real sensor noise, without relying on simplified parametric models or large-scale data acquisition. The method is data-efficient, computationally lightweight, and can be applied to different sensors without extensive calibration.

Despite these advances, some limitations remain. Some components of signal-independent noise are influenced by factors beyond ISO, such as sensor temperature, exposure duration, and readout timing. For instance, dark current increases with temperature, and black level error may drift slightly as the sensor warms up. In our current formulation, we assume stable imaging conditions and model noise variations primarily with respect to ISO, without explicitly accounting for temperature or exposure time. Extending the method to incorporate these factors is an interesting direction for future work.

References

- [1] Abdelrahman Abdelhamed, Stephen Lin, and Michael S Brown. A high-quality denoising dataset for smartphone cameras. In *Proceedings of the IEEE conference on computer vision and pattern recognition*, pages 1692–1700, 2018.
- [2] Abdelrahman Abdelhamed, Marcus A Brubaker, and Michael S Brown. Noise flow: Noise modeling with conditional normalizing flows. In *Proceedings of the IEEE/CVF International Conference on Computer Vision*, pages 3165–3173, 2019.
- [3] Josue Anaya and Adrian Barbu. Renoir—a dataset for real low-light image noise reduction. *Journal of Visual Communication and Image Representation*, 51:144–154, 2018.
- [4] Nicolas Bähler, Majed El Helou, Étienne Objois, Kaan Okumuş, and Sabine Süsstrunk. Pogain: Poisson-gaussian image noise modeling from paired samples. *IEEE Signal Processing Letters*, 29:2602–2606, 2022.
- [5] Tim Brooks, Ben Mildenhall, Tianfan Xue, Jiawen Chen, Dillon Sharlet, and Jonathan T Barron. Unprocessing images for learned raw denoising. In *Proceedings of the IEEE/CVF Conference on Computer Vision and Pattern Recognition*, pages 11036–11045, 2019.
- [6] Antoni Buades, Bartomeu Coll, and J-M Morel. A non-local algorithm for image denoising. In *2005 IEEE computer society conference on computer vision and pattern recognition (CVPR’05)*, volume 2, pages 60–65. Ieee, 2005.
- [7] Stephen C Cain, Majeed M Hayat, and Ernest E Armstrong. Projection-based image registration in the presence of fixed-pattern noise. *IEEE Transactions on Image Processing*, 10(12):1860–1872, 2001.
- [8] Yue Cao, Ming Liu, Shuai Liu, Xiaotao Wang, Lei Lei, and Wangmeng Zuo. Physics-guided iso-dependent sensor noise modeling for extreme low-light photography. In *Proceedings of the IEEE/CVF Conference on Computer Vision and Pattern Recognition*, pages 5744–5753, 2023.
- [9] Chen Chen, Qifeng Chen, Jia Xu, and Vladlen Koltun. Learning to see in the dark. In *Proceedings of the IEEE conference on computer vision and pattern recognition*, pages 3291–3300, 2018.
- [10] Roberto Costantini and Sabine Süsstrunk. Virtual sensor design. In *Sensors and Camera Systems for Scientific, Industrial, and Digital Photography Applications V*, volume 5301, pages 408–419. SPIE, 2004.
- [11] Laurent Dinh, Jascha Sohl-Dickstein, and Samy Bengio. Density estimation using real nvp. *arXiv preprint arXiv:1605.08803*, 2016.
- [12] Hansen Feng, Lizhi Wang, Yuzhi Wang, Haoqiang Fan, and Hua Huang. Learnability enhancement for low-light raw image denoising: A data perspective. *IEEE Transactions on Pattern Analysis and Machine Intelligence*, 46(1):370–387, 2023.
- [13] Roman Flepp, Andrey Ignatov, Radu Timofte, and Luc Van Gool. Real-world mobile image denoising dataset with efficient baselines. In *Proceedings of the IEEE/CVF Conference on Computer Vision and Pattern Recognition*, pages 22368–22377, 2024.
- [14] Alessandro Foi. Clipped noisy images: Heteroskedastic modeling and practical denoising. *Signal Processing*, 89(12):2609–2629, 2009.
- [15] Alessandro Foi, Mejd Trimeche, Vladimir Katkovnik, and Karen Egiazarian. Practical poissonian-gaussian noise modeling and fitting for single-image raw-data. *IEEE Transactions on Image Processing*, 17(10):1737–1754, 2008.
- [16] Bruno Galerne, Yann Gousseau, and Jean-Michel Morel. Random phase textures: Theory and synthesis. *IEEE Transactions on image processing*, 20(1): 257–267, 2010.
- [17] Ryan D Gow, David Renshaw, Keith Findlater, Lindsay Grant, Stuart J McLeod, John Hart, and Robert L Nicol. A comprehensive tool for modeling cmos image-sensor-noise performance. *IEEE Transactions on Electron Devices*, 54(6):1321–1329, 2007.
- [18] Shuhang Gu, Lei Zhang, Wangmeng Zuo, and Xianguang Feng. Weighted nuclear norm minimization with application to image denoising. In *Proceedings of the IEEE conference on computer vision and pattern recognition*, pages 2862–2869, 2014.
- [19] Ishaan Gulrajani, Faruk Ahmed, Martin Arjovsky, Vincent Dumoulin, and Aaron C Courville. Improved training of wasserstein gans. *Advances in Neural Information Processing Systems*, 30, 2017.

- [20] Glenn E Healey and Raghava Kondepudy. Radiometric ccd camera calibration and noise estimation. *IEEE Transactions on Pattern Analysis and Machine Intelligence*, 16(3):267–276, 2002.
- [21] Gerald C Holst and Lomheim GC. *CMOS/CCD Sensors*. JCD publishing, 2007.
- [22] Brian L Joiner and Joan R Rosenblatt. Some properties of the range in samples from tukey’s symmetric lambda distributions. *Journal of the American Statistical Association*, 66(334):394–399, 1971.
- [23] Durk P Kingma and Prafulla Dhariwal. Glow: Generative flow with invertible 1x1 convolutions. *Advances in Neural Information Processing Systems*, 31, 2018.
- [24] Ivan Kobyzev, Simon JD Prince, and Marcus A Brubaker. Normalizing flows: An introduction and review of current methods. *IEEE Transactions on Pattern Analysis and Machine Intelligence*, 43(11):3964–3979, 2020.
- [25] Mikhail Konnik and James Welsh. High-level numerical simulations of noise in ccd and cmos photosensors: review and tutorial. *arXiv preprint arXiv:1412.4031*, 2014.
- [26] Shayan Kousha, Ali Maleky, Michael S Brown, and Marcus A Brubaker. Modeling srgb camera noise with normalizing flows. In *Proceedings of the IEEE/CVF Conference on Computer Vision and Pattern Recognition*, pages 17463–17471, 2022.
- [27] John-Peter Lewis. Texture synthesis for digital painting. In *Proceedings of the 11th annual conference on Computer graphics and interactive techniques*, pages 245–252, 1984.
- [28] Jingyun Liang, Jiezhong Cao, Guolei Sun, Kai Zhang, Luc Van Gool, and Radu Timofte. Swinir: Image restoration using swin transformer. In *Proceedings of the IEEE/CVF international conference on computer vision*, pages 1833–1844, 2021.
- [29] Liying Lu, Raphael Achddou, and Sabine Susstrunk. Dark noise diffusion: Noise synthesis for low-light image denoising. *IEEE Transactions on Pattern Analysis and Machine Intelligence*, 2025.
- [30] Xiaojiao Mao, Chunhua Shen, and Yu-Bin Yang. Image restoration using very deep convolutional encoder-decoder networks with symmetric skip connections. *Advances in neural information processing systems*, 29, 2016.
- [31] Lars Mescheder, Andreas Geiger, and Sebastian Nowozin. Which training methods for gans do actually converge? In *International Conference on Machine Learning*, pages 3481–3490. PMLR, 2018.
- [32] Kristina Monakhova, Stephan R Richter, Laura Waller, and Vladlen Koltun. Dancing under the stars: video denoising in starlight. In *Proceedings of the IEEE/CVF Conference on Computer Vision and Pattern Recognition*, pages 16241–16251, 2022.
- [33] Junichi Nakamura. *Image sensors and signal processing for digital still cameras*. CRC press, 2017.
- [34] Aditya Ramesh, Prafulla Dhariwal, Alex Nichol, Casey Chu, and Mark Chen. Hierarchical text-conditional image generation with clip latents. *arXiv preprint arXiv:2204.06125*, 1(2):3, 2022.
- [35] Robin Rombach, Andreas Blattmann, Dominik Lorenz, Patrick Esser, and Björn Ommer. High-resolution image synthesis with latent diffusion models. In *Proceedings of the IEEE/CVF Conference on Computer Vision and Pattern Recognition*, pages 10684–10695, 2022.
- [36] Jarke J Van Wijk. Spot noise texture synthesis for data visualization. In *Proceedings of the 18th annual conference on Computer graphics and interactive techniques*, pages 309–318, 1991.
- [37] Hans B Wach and Edward R Dowski. Noise modeling for design and simulation of color imaging systems. In *Color and Imaging Conference*, volume 12, pages 211–216. Society of Imaging Science and Technology, 2004.
- [38] Kaixuan Wei, Ying Fu, Yinqiang Zheng, and Jiaolong Yang. Physics-based noise modeling for extreme low-light photography. *IEEE Transactions on Pattern Analysis and Machine Intelligence*, 44(11):8520–8537, 2021.
- [39] Syed Waqas Zamir, Aditya Arora, Salman Khan, Munawar Hayat, Fahad Shahbaz Khan, and Ming-Hsuan Yang. Restormer: Efficient transformer for high-resolution image restoration. In *Proceedings of the IEEE/CVF conference on computer vision and pattern recognition*, pages 5728–5739, 2022.
- [40] Feng Zhang, Bin Xu, Zhiqiang Li, Xinran Liu, Qingbo Lu, Changxin Gao, and Nong Sang. Towards general low-light raw noise synthesis and modeling. In *Proceedings of the IEEE/CVF International Conference on Computer Vision*, pages 10820–10830, 2023.
- [41] Jiachao Zhang and Keigo Hirakawa. Improved denoising via poisson mixture modeling of image sensor noise. *IEEE Transactions on Image Processing*, 26(4):1565–1578, 2017.
- [42] Kai Zhang, Wangmeng Zuo, Yunjin Chen, Deyu Meng, and Lei Zhang. Beyond a gaussian denoiser: Residual learning of deep cnn for image denoising. *IEEE transactions on image processing*, 26(7):3142–3155, 2017.
- [43] Kai Zhang, Wangmeng Zuo, and Lei Zhang. Ffdnet: Toward a fast and flexible solution for cnn-based image denoising. *IEEE Transactions on Image Processing*, 27(9):4608–4622, 2018.
- [44] Kai Zhang, Yawei Li, Wangmeng Zuo, Lei Zhang, Luc Van Gool, and Radu Timofte. Plug-and-play image

restoration with deep denoiser prior. *IEEE Transactions on Pattern Analysis and Machine Intelligence*, 44 (10):6360–6376, 2021.

- [45] Yi Zhang, Hongwei Qin, Xiaogang Wang, and Hongsheng Li. Rethinking noise synthesis and modeling in raw denoising. In *Proceedings of the IEEE/CVF International Conference on Computer Vision*, pages 4593–4601, 2021.

Appendix

This appendix is organized as follows:

- Method Details → Sec. A
 - Spectral Sampling Algorithm → Sec. A.1
 - Photon Noise Parameter Estimation → Sec. A.2
- More Implementation Details → Sec. B
 - Data Synthesis Details → Sec. B.1
 - Training Details → Sec. B.2
 - Evaluation Details → Sec. B.3
- More Discussions → Sec. C
 - Effect of the Fixed-Pattern Removal Before Sampling → Sec. C.1
 - Importance of Inter-Channel Correlation → Sec. C.2
 - Effect of Iterative Histogram Matching → Sec. C.3
 - Different Ways to Leverage a Single Dark Frame → Sec. C.4
 - Realism Validation of Synthetic Data → Sec. C.5
 - Photon Noise Parameter Estimation with Limited Data → Sec. C.6
- Synthetic Noise Visualization Across Different Sensors → Sec. D
- More Visual Comparisons → Sec. E

For optimal visual comparisons, we recommend viewing the results on a screen.

A Method Details

A.1 Spectral Sampling Algorithm

The full procedure of our spectral sampling algorithm for dark-frame synthesis is summarized in Algorithm 1.

A.2 Photon Noise Parameter Estimation

In Sec. 3.2 of the main paper, we have shown that the noisy observation y can be modeled as:

$$y = g\mathcal{P}(x) + n_{\text{other}}. \quad (16)$$

For a Poisson random variable, the variance equals its mean, i.e., $\text{Var}(\mathcal{P}(x)) = x$. Thus the variance of the noisy observation is:

$$\begin{aligned} \text{Var}(y) &= g^2 \text{Var}(\mathcal{P}(x)) + \text{Var}(n_{\text{other}}) \\ &= g^2 x + \text{Var}(n_{\text{other}}) \\ &= g(gx) + \text{Var}(n_{\text{other}}). \end{aligned} \quad (17)$$

Consequently, the system gain g can be estimated by performing a linear fit between the variance of the noisy observation y and the amplified clean signal gx , using a set of clean-noisy pairs. If only a single noisy image is available, a rough estimate of g can still be obtained. Specifically, we unfold the noisy image into overlapping 3×3 patches. For each patch, we apply a Gaussian blur to obtain a pseudo-clean value, and all pixels within the patch serve as noisy observations from which the noise variance is computed. Patches sharing the same mean value are then grouped together to produce more robust variance estimates.

Of course, more sophisticated approaches can be used for pseudo-clean estimation when needed, and additional data can possibly further improve accuracy. For example, when flat-field frames are available (*e.g.*, a uniform calibration card illuminated by a single light source), a more reliable estimation of g can be obtained by following the procedures described in [12, 20, 38].

B More Implementation Details

B.1 Data Synthesis Details

In the LRID dataset [12], two types of dark frames of ISO=6400 are provided: one captured under normal sensor temperature and the other in the sensor’s hot mode. For noise synthesis, we use a single dark frame from each setting to generate the corresponding synthetic dark frames. The synthesis results are shown in Fig. 14.

B.2 Training Details

We use the same U-Net architecture as [9] for all denoising experiments. The networks are trained for 500 epochs using the Adam optimizer. The initial learning rate is set to 2×10^{-4} , reduced by half at epoch 250, and fixed to 1×10^{-5} after epoch 400. During training, we use a batch size of 4 and randomly crop 256×256 patches with random horizontal flips for data augmentation. We train the denoisers using the L_1 loss between the network output and the clean reference image.

B.3 Evaluation Details

Since Peak Signal-to-Noise Ratio (PSNR) and Structural Similarity (SSIM) are sensitive to global illumination, even small brightness shifts can cause large metric variations. During denoising inference, we apply the illumination correction

method from the ELD paper [38] to the denoised images. We apply this illumination correction to all compared methods before evaluating PSNR and SSIM. We compute the PSNR and SSIM between the denoised and reference images in the RAW domain.

C More Discussions

C.1 Effect of the Fixed-Pattern Removal Before Sampling

Dark frames contain both deterministic fixed patterns and stochastic noise components. Directly applying spectral analysis to raw dark frames would conflate these two components: the low-frequency fixed patterns would dominate the power spectrum, biasing the estimated noise statistics and leading to synthesized noise that incorrectly replicates deterministic sensor artifacts as if they were stochastic variations.

To isolate the stochastic component for spectral modeling, we apply Gaussian blur (Eq. 1) to extract the fixed pattern, then work with the residual. Figure 7 demonstrates the effect of fixed-pattern removal for noise synthesis. Given a real dark frame, without fixed-pattern removal, the synthesized noise (bottom-left) incorrectly produces random patterns of the deterministic fixed pattern, failing to produce faithful results. With appropriate blur kernel sizes, the method successfully separates the two components. We empirically find that choosing σ in the range of $[40, 60]$ consistently yields good results. We set $\sigma = 50$ in our experiments.

C.2 Importance of Inter-Channel Correlation

Fig. 10 presents additional ablation results for the inter-channel correlation ICC. Without ICC, the denoised images exhibit noticeable residual banding artifacts, whereas our full method produces cleaner results.

C.3 Effect of Iterative Histogram Matching

In the main paper, we mentioned that we perform K iterations of histogram matching. Here, we study how the choice of K influences the accuracy of the synthesized noise. In Fig. 8, we show the relationship between the Kullback–Leibler divergence (KLD) between the synthetic and real noise and the value of K . As K increases, the synthetic noise progressively converges toward the real noise distribution, reflected by the decreasing KLD. We set $K = 10$ in our experiments.

In the main paper, we showed that iterative histogram matching (IHM) reduces color distortions in denoised results. Beyond this, we also find that IHM helps suppress saturated malfunctioning pixels. As shown in Fig. 11, without IHM, noticeable white spots appear in the denoised outputs due to saturated pixels in the noisy inputs. With our full method, this issue is effectively mitigated.

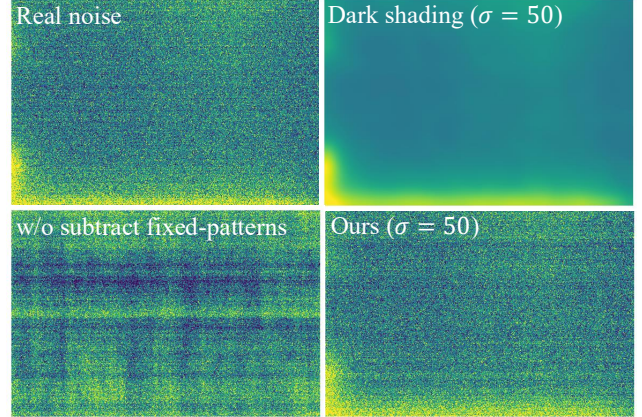


Figure 7: Effect of fixed-pattern removal before noise synthesis. Left: Real dark frame at ISO 12800 (top) and synthesized noise without fixed-pattern removal (bottom), which incorrectly reproduces deterministic row/column structure. Right: The estimated fixed-pattern component (top) and the synthesized noise after removing it prior to spectral sampling (bottom), resulting in a more realistic stochastic noise pattern.

C.4 Different Ways to Leverage a Single Dark Frame

Given one single dark frame, we study the three different ways to leverage it for data synthesis: *DirectAdd*, *RandomCrop*, and *Ours*. In Fig. 12, we show two denoising examples, our method produces cleaner results with fewer artifacts.

C.5 Realism Validation of Synthetic Data

To further evaluate the realism of our synthetic noise, we train a denoising network (*RealDF*) using all available real dark frames from each ISO level in the SID dataset. For fair comparison, we generate one synthetic dark frame per real dark frame, ensuring identical data volume and ISO distribution, and train another denoising network (*SynDF*). The same protocol is applied to the LRID dataset. Fig. 9 shows the PSNR difference between *RealDF* and *SynDF* on the SID, ELD and LRID test set across different exposure ratios. The differences are consistently close to zero across all datasets and ratios, indicating that our method can synthesize noise distributions nearly indistinguishable from real sensor noise.

C.6 Photon Noise Parameter Estimation with Limited Data

In our experiments, we assume only a single noisy image per ISO is available for system gain estimation. To assess the effect of data availability, we compare denoising performance on the SID and ELD test sets when g is estimated using either one noisy image or 16 clean–noisy pairs.

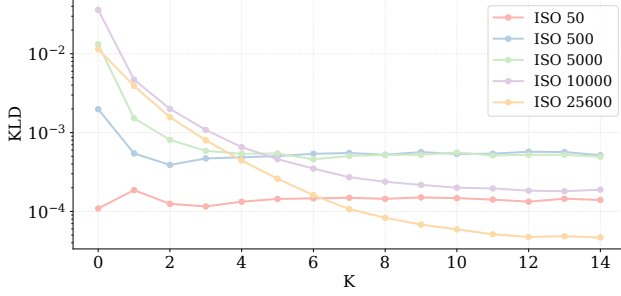


Figure 8: Relationship between the Kullback–Leibler divergence (KLD) between the synthetic and real noise and the histogram matching iteration number K , across different ISO settings. Increasing K generally reduces the KLD.

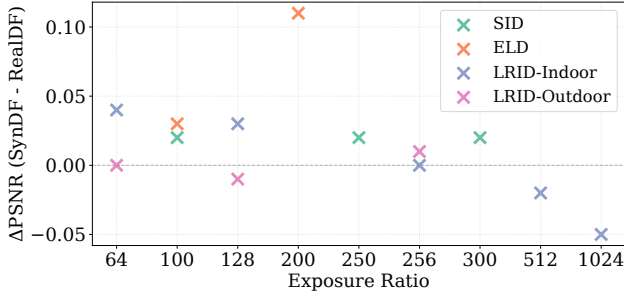


Figure 9: PSNR differences between *RealDF* and *SynDF* across different exposure ratios for the SID, ELD, and LRID test sets. Each \times denotes the result of a subset of each test set, e.g., the left-most \times denotes that the PSNR difference between *RealDF* and *SynDF* on the LRID-Indoor dataset with exposure Ratio = 64 is almost 0, indicating that our method can synthesize noise distributions nearly indistinguishable from real sensor noise.

As shown in Table 5, using a single noisy image leads to a slight drop in performance under some settings compared to using multiple clean–noisy pairs. While our study focuses on the single noisy image scenario, access to additional data, such as multiple clean–noisy pairs or flat-field frames, could potentially improve the accuracy of gain estimation and denoising results.

D Synthetic Noise Visualization Across Different Sensors

In this section, we visualize examples of real dark frames from various sensors alongside our synthesized dark frames. Figures 13 and 14 show examples from the Sony A7S2 sensor and the IMX686 sensor in the Redmi K30 smartphone, respectively. We also captured dark frames using a Fujifilm X-M5 camera, whose RAW images follow the X-Trans pat-

tern instead of the Bayer pattern. Fig. 15 presents the real dark frames and our synthetic results. It can be observed that our method successfully generates realistic dark frames across different sensors, demonstrating its generalizability.

E More Visual Comparisons

In this section, we provide more visual comparisons of denoising results from different denoisers trained on data synthesized using different methods. Fig. 16, Fig. 17 and Fig. 18 are examples from the SID test set. Fig. 19 are examples from the ELD test set. Fig. 20 and Fig. 21 are examples from the LRID test set.

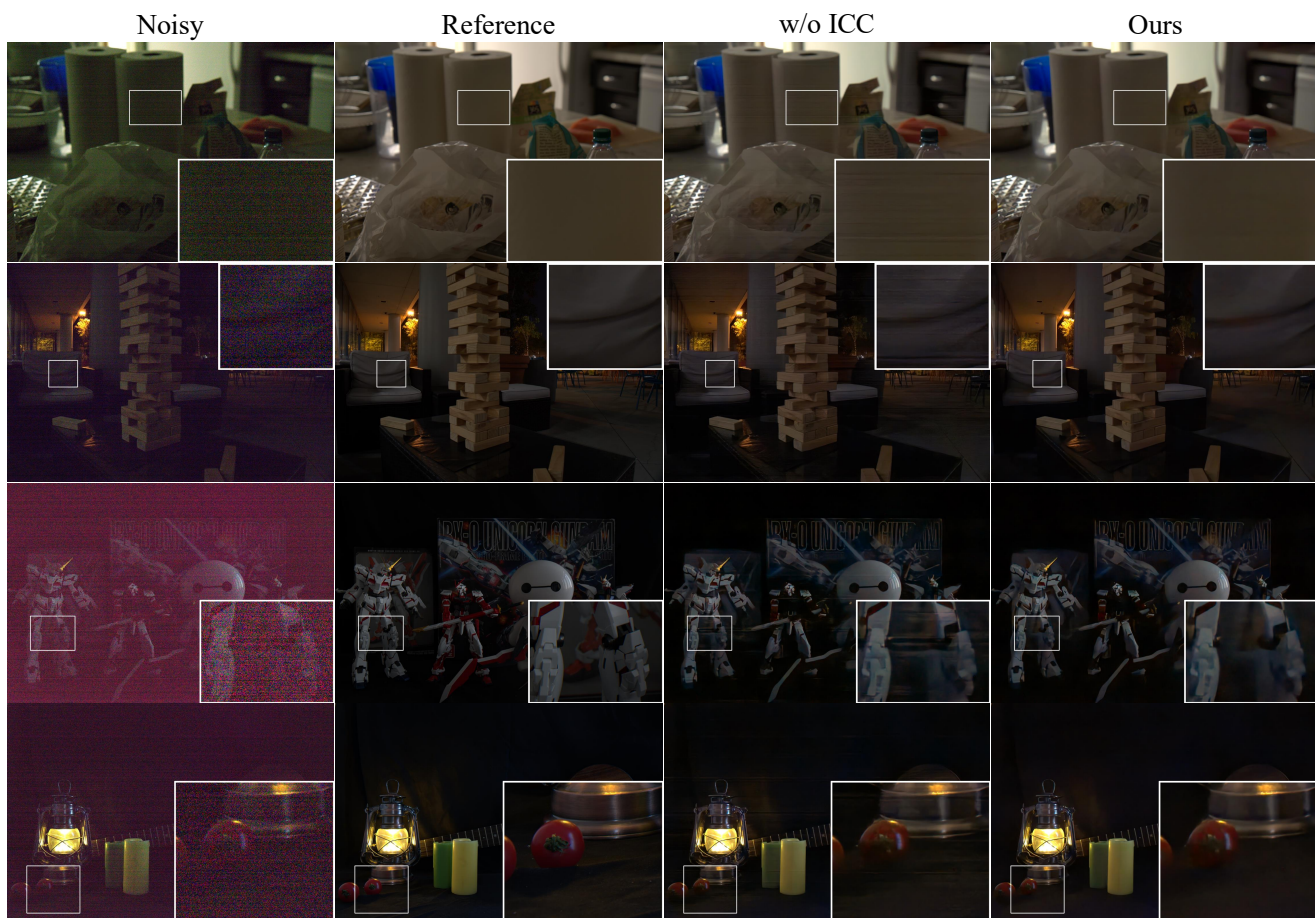


Figure 10: Ablation study on inter-channel correlation (ICC). Without ICC, the denoised results show residual banding artifacts, while our full method produces clean outputs. The first two examples are from the SID test set, and the third and fourth are from the ELD test set. Best viewed when zoomed in.



Figure 11: Ablation study on the iterative histogram matching (IHM). Without IHM, noticeable white spots appear in the denoised outputs due to saturated pixels in the noisy inputs. With our full method, this issue is effectively mitigated. The first two examples are from the SID test set while the third and forth are from the ELD test set. Best viewed zoomed in.

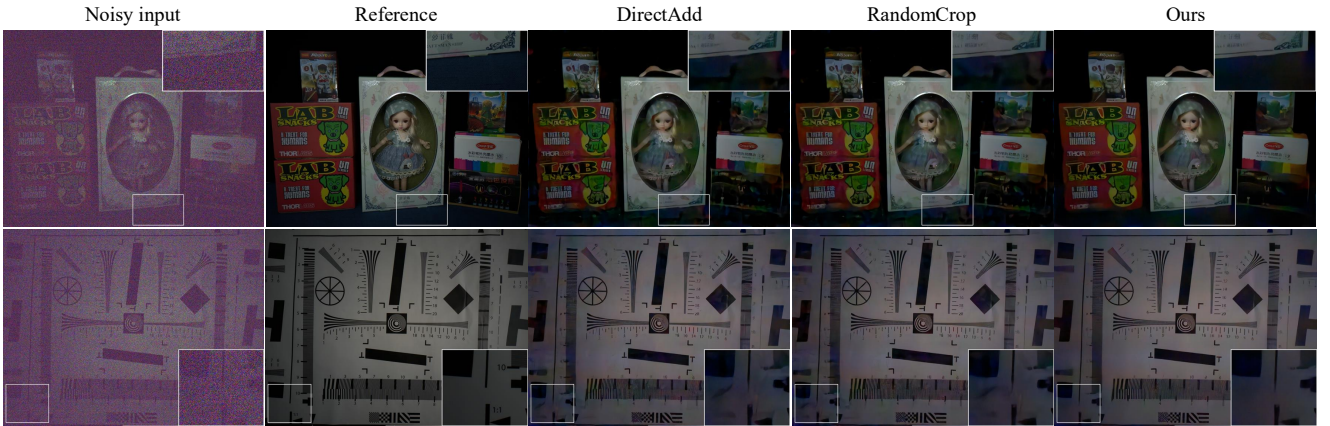


Figure 12: Denoising results of the network trained with different data sources synthesized using only one real dark frame per ISO setting. Our method produces cleaner results with less artifacts.

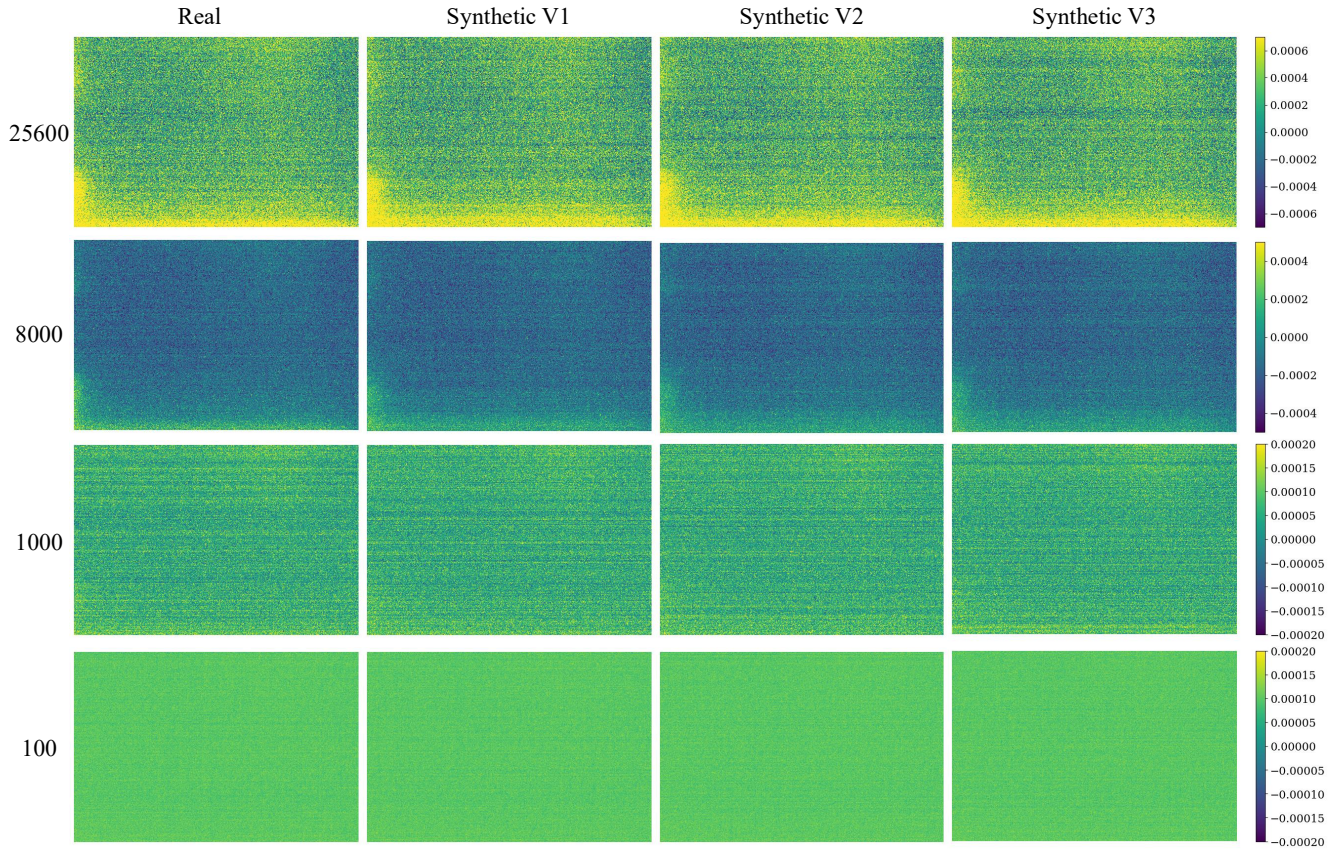


Figure 13: Real dark frames and three different synthetic dark frame realizations (generated with different random seeds) across various ISO settings (ISO=25600, 8000, 1000, 100) of the Sony A7S2 sensor.

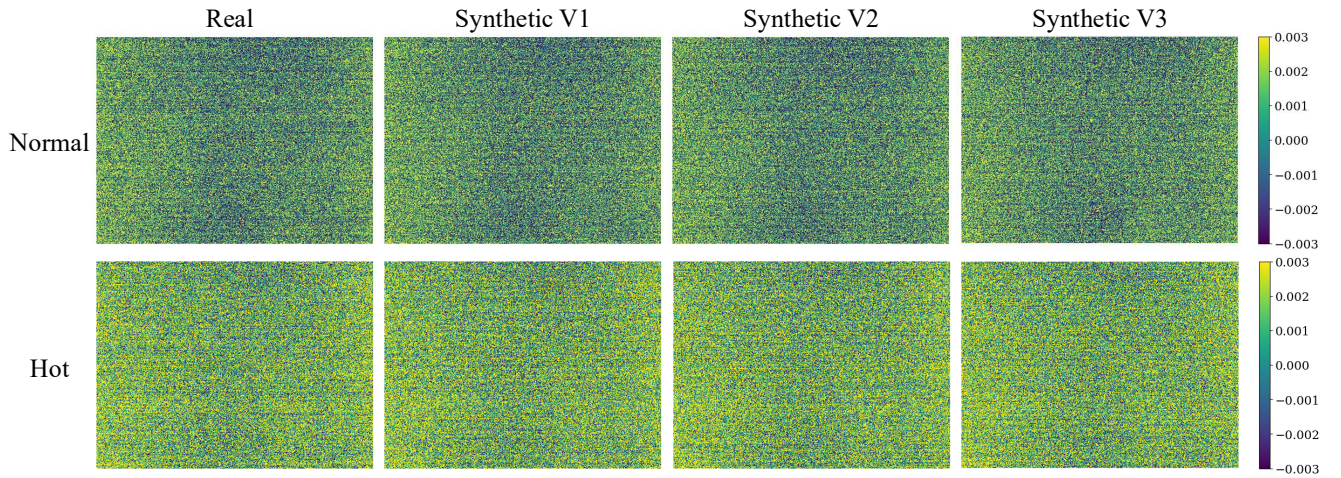


Figure 14: Real dark frames and three different synthetic dark frame realizations (generated with different random seeds) with ISO=6400 of the IMX686 sensor. The first example is captured under normal sensor temperature and the second in the sensor's hot mode.

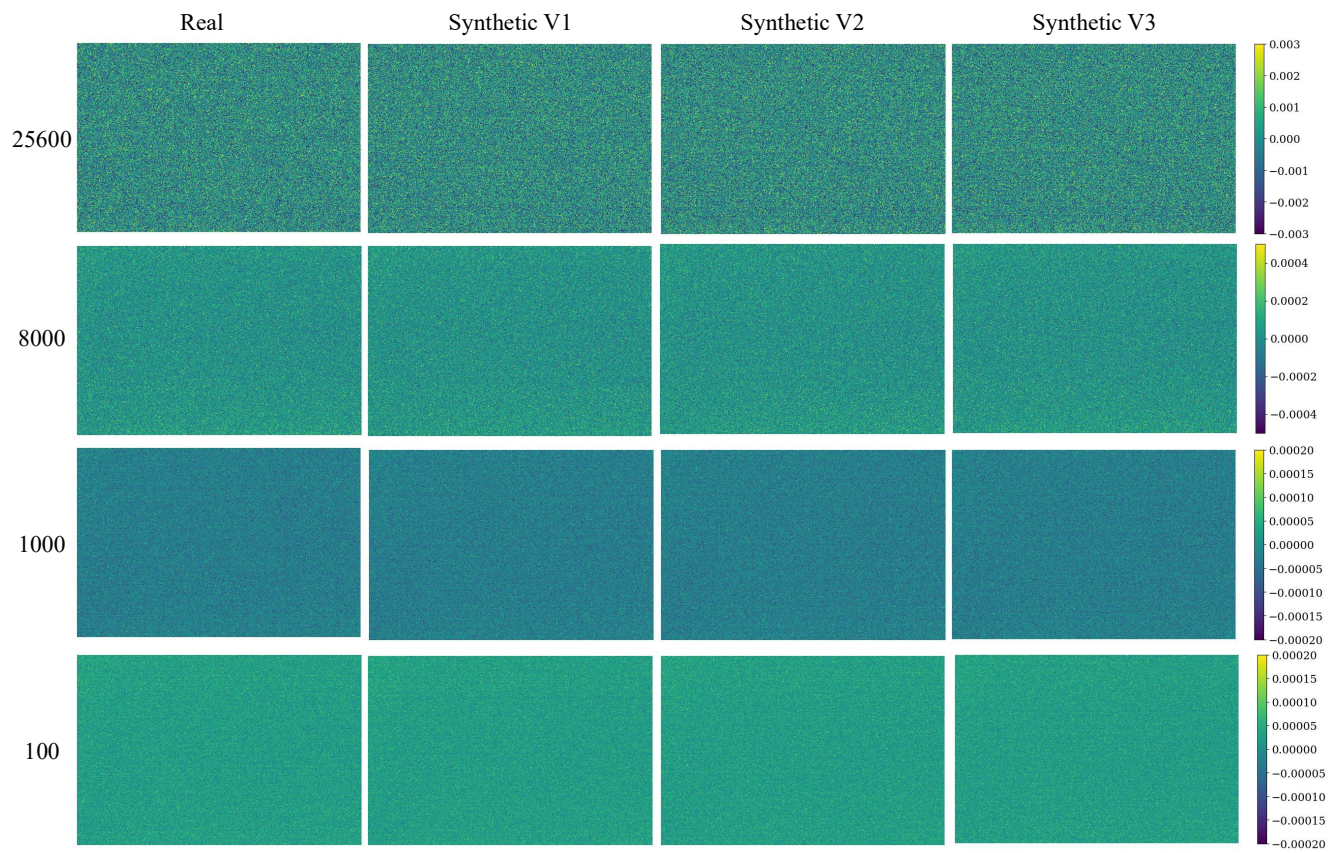


Figure 15: Real dark frames and three different synthetic dark frame realizations (generated with different random seeds) across various ISO settings (ISO=25600, 8000, 1000, 100) of the Fujifilm X-M5 sensor.

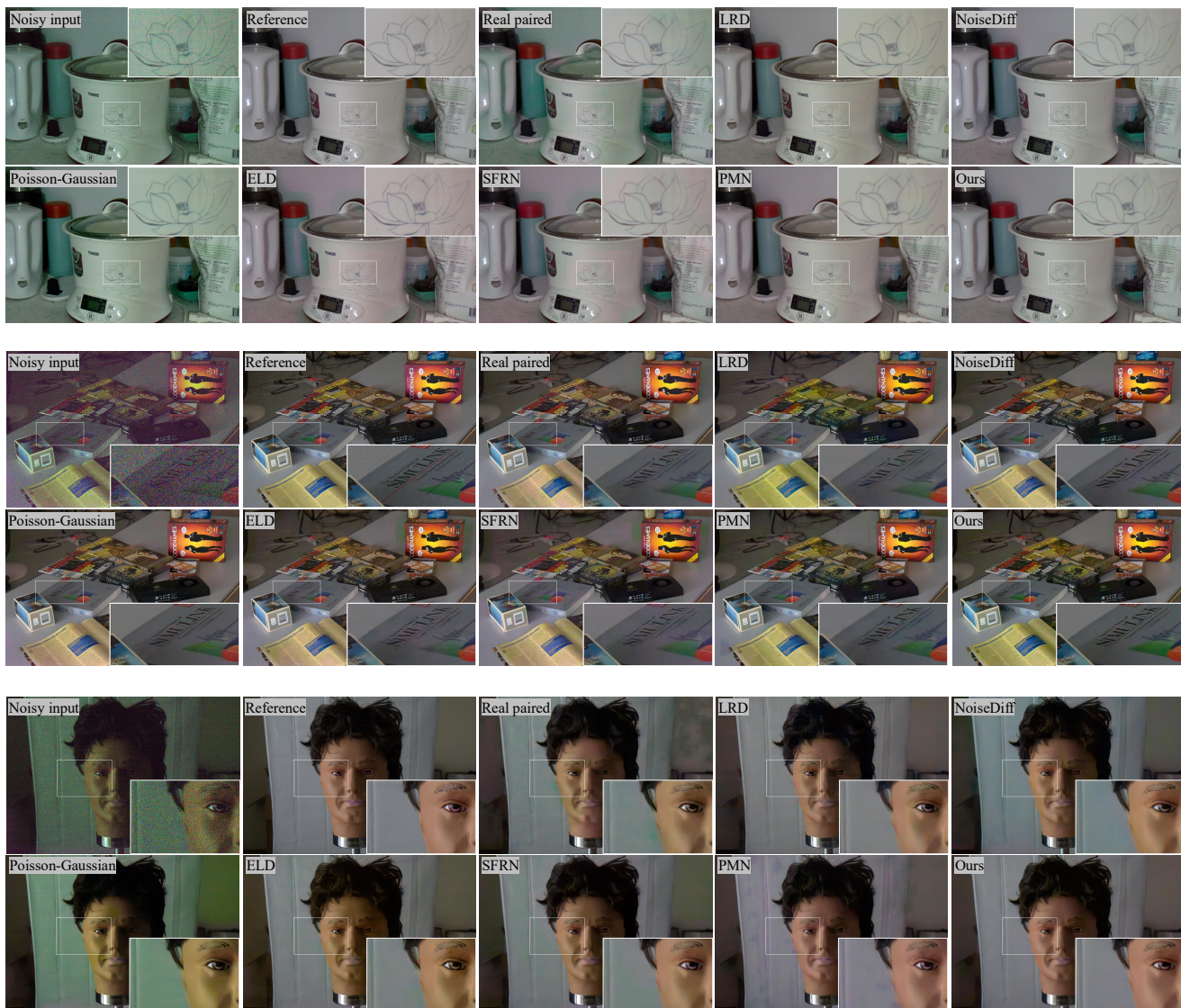


Figure 16: Result comparison of denoisers trained on data synthesized using different methods on the SID test set.

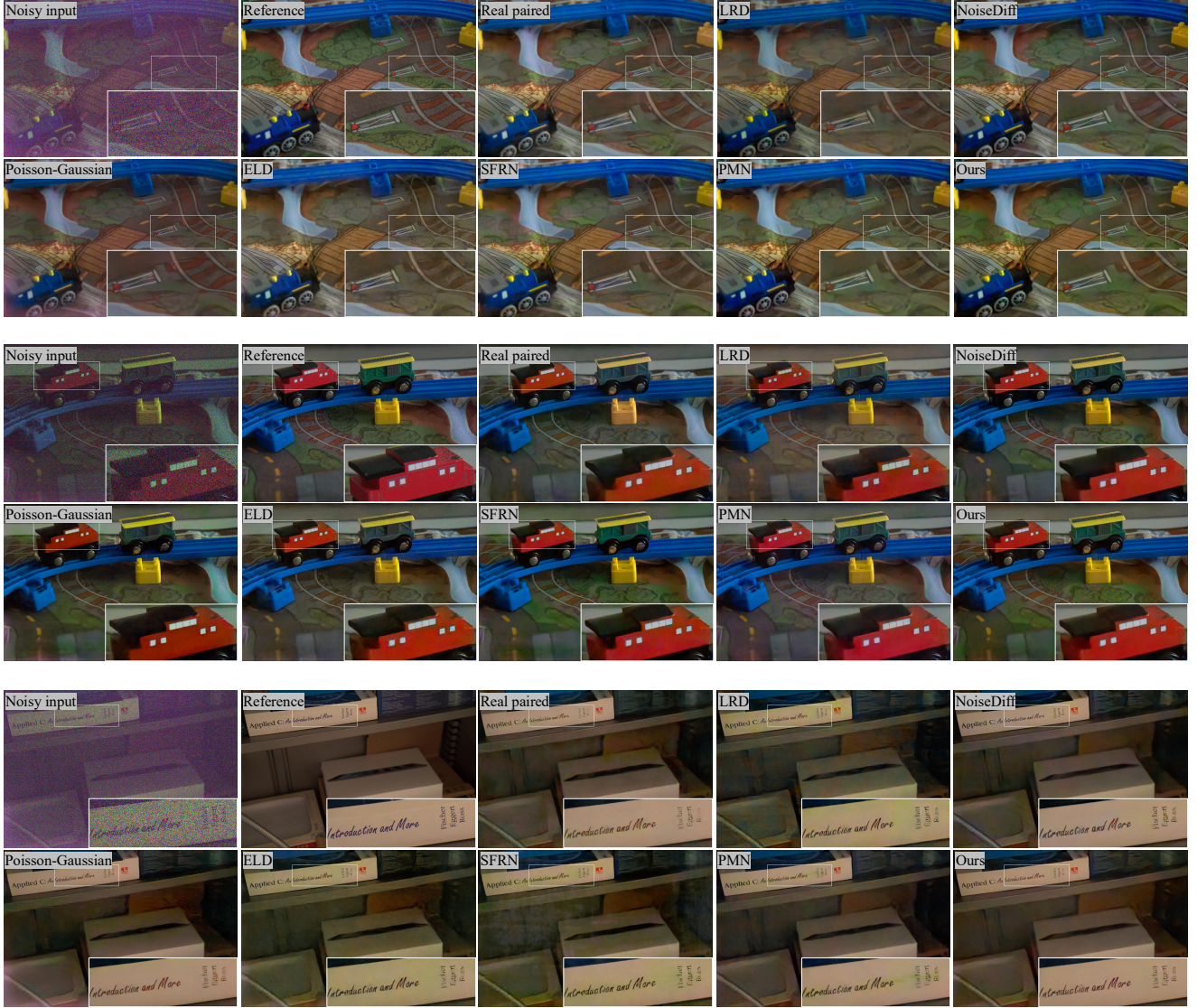


Figure 17: Result comparison of denoisers trained on data synthesized using different methods on the SID test set.



Figure 18: Result comparison of denoisers trained on data synthesized using different methods on the SID test set.

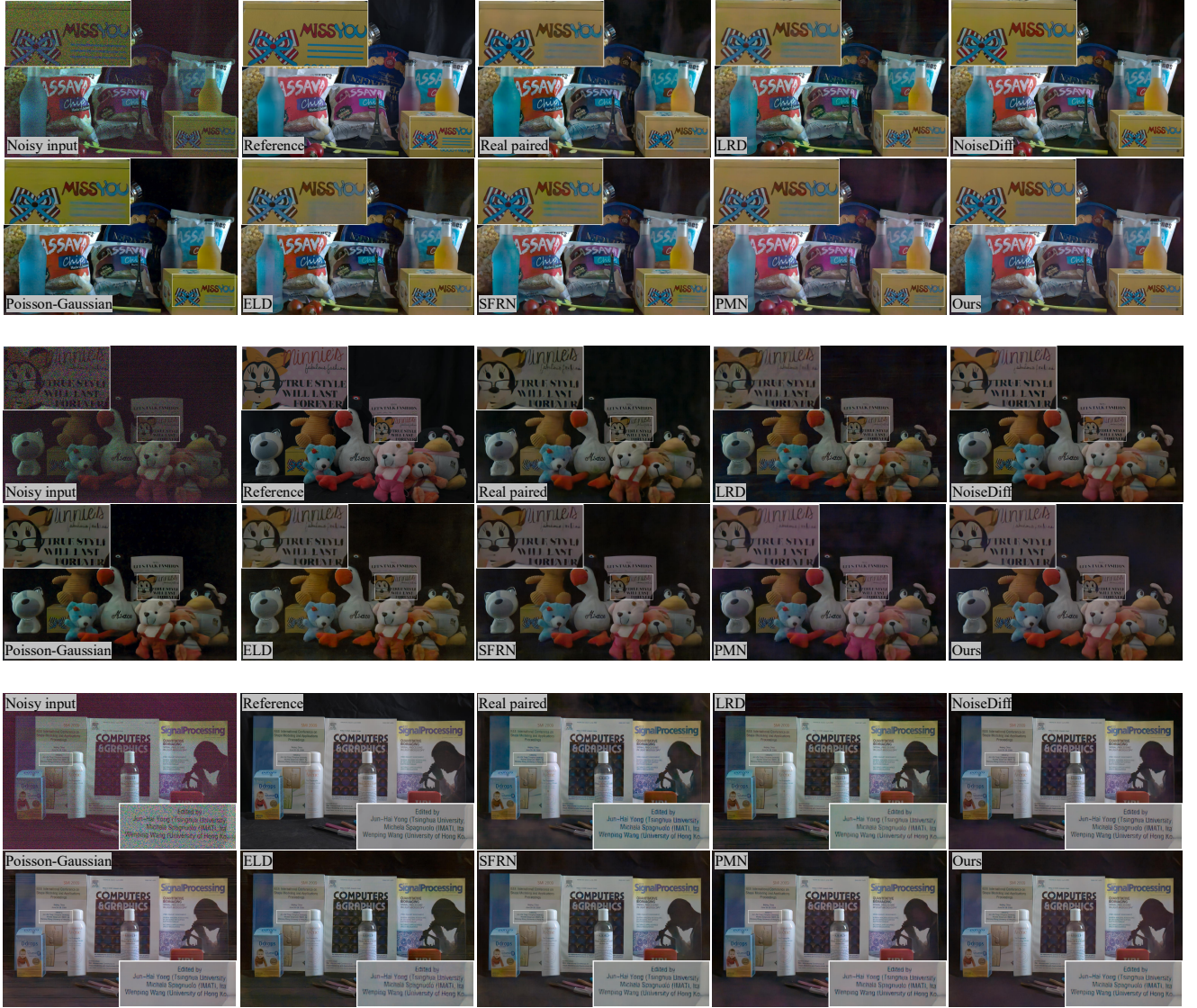


Figure 19: Result comparison of denoisers trained on data synthesized using different methods on the ELD test set. Images are gamma-corrected ($\gamma = 1.4$) for better visibility.

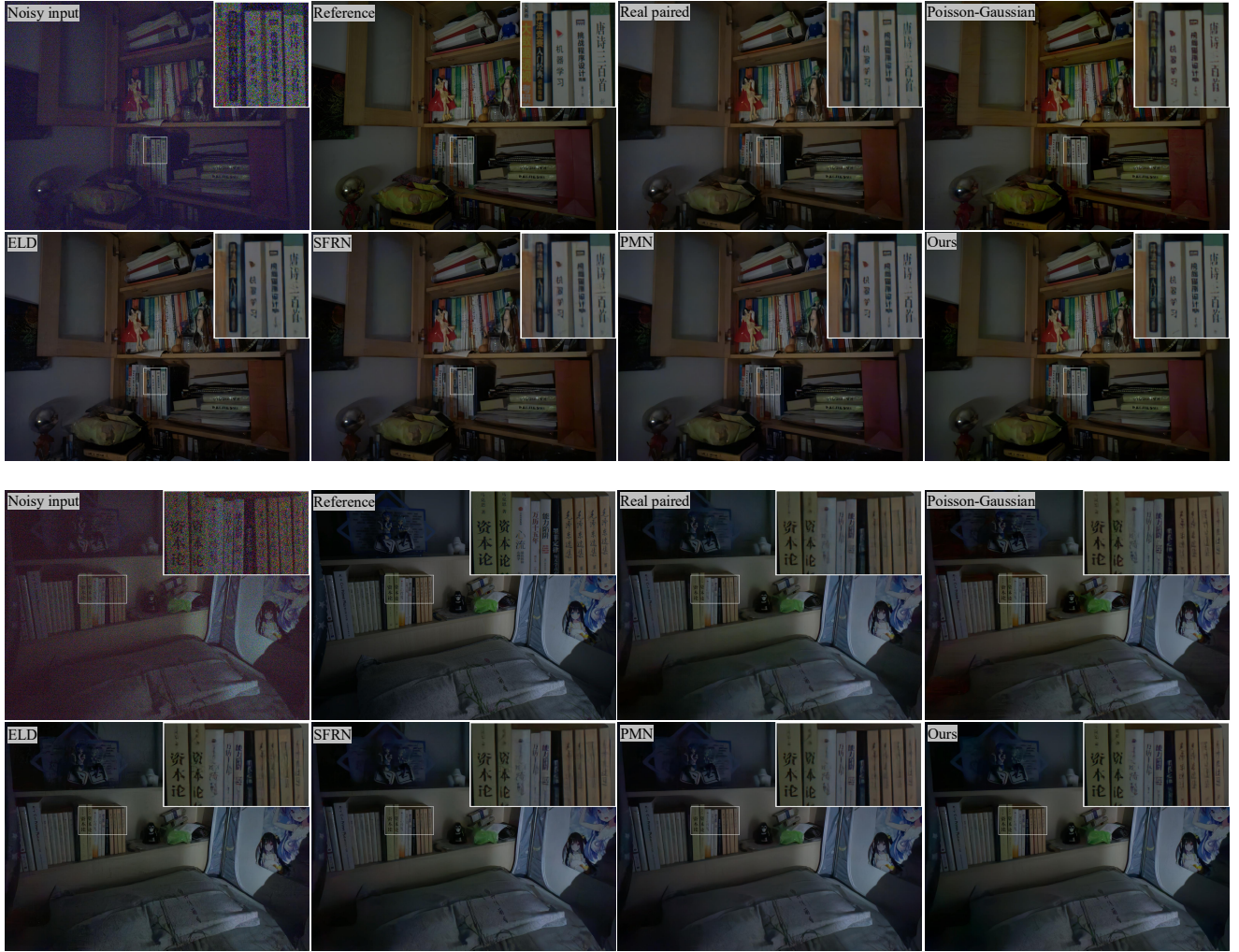


Figure 20: Result comparison of denoisers trained on data synthesized using different methods on the LRID test set.

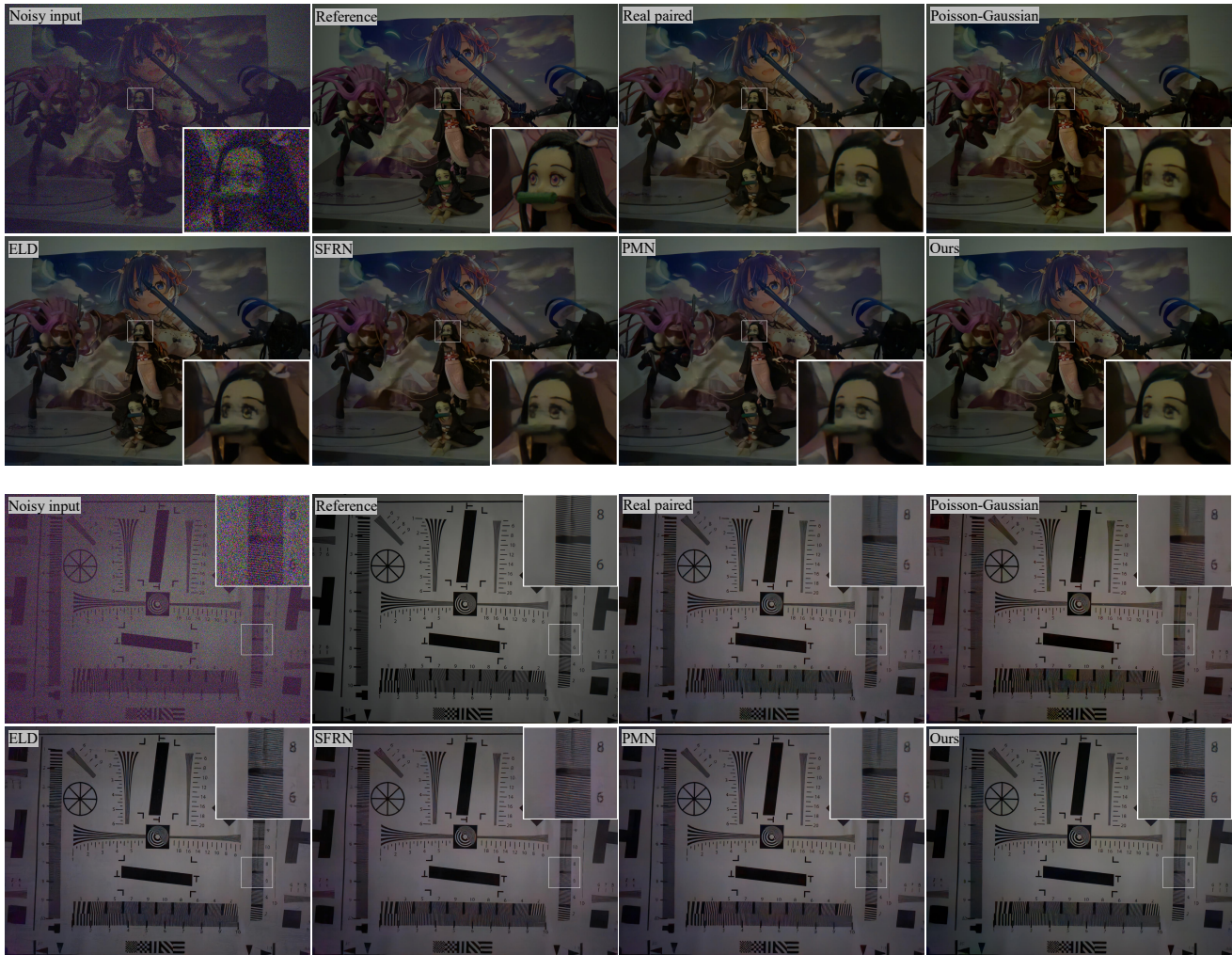


Figure 21: Result comparison of denoisers trained on data synthesized using different methods on the LRID test set.

Algorithm 1: Spectral Sampling with Iterative Refinement for Dark Frame Synthesis

Input: Reference dark frame $I_{\text{dark}} \in \mathbb{R}^{C \times H \times W}$,
Gaussian blur parameter σ , number of
iterations K

Output: Synthesized dark frame \tilde{I}_{dark}

Step 1: Fixed-pattern removal

$$S \leftarrow \mathcal{G}_\sigma(I_{\text{dark}}); \quad // \text{ Extract low-frequency pattern}$$

$$R' \leftarrow I_{\text{dark}} - S; \quad // \text{ Isolate stochastic residual}$$

$$\mu^R \leftarrow \mathbb{E}[R']; \quad // \text{ Compute channel-wise mean}$$

$$R \leftarrow R' - \mu^R; \quad // \text{ Center to zero mean}$$

Step 2: Spectral prior estimation

$$\hat{R} \leftarrow \mathcal{F}\{R\}; \quad // \text{ Compute reference spectrum}$$

Step 3: Phase randomization

$$\xi^0 \sim \mathcal{U}([-\pi, \pi]^{(H,W)}); \quad // \text{ Uniform random phase}$$

$$\xi \leftarrow \text{replicate}(\xi^0, C); \quad // \text{ Copy across channels}$$

$$\hat{N} \leftarrow |\hat{R}| \odot \exp(i(\theta_{\hat{R}} + \xi)); \quad // \text{ Phase Randomization}$$

$$N^{(0)} \leftarrow \frac{1}{\sqrt{HW}} \mathcal{F}^{-1}\{\hat{N}\}; \quad // \text{ Initial synthesis}$$

Step 4: Iterative histogram-spectral refinement

for $k = 0$ to $K - 1$ do

$$N_{\text{hist}}'^{(k)} \leftarrow \mathcal{H}(N^{(k)}, R); \quad // \text{ Match Hist.}$$

$$\mu_{\text{hist}}^{(k)} \leftarrow \mathbb{E}[N_{\text{hist}}'^{(k)}]$$

$$N_{\text{hist}}^{(k)} \leftarrow N_{\text{hist}}'^{(k)} - \mu_{\text{hist}}^{(k)}$$

$$\hat{N}_{\text{hist}}^{(k)} \leftarrow \mathcal{F}\{N_{\text{hist}}^{(k)}\}$$

$$\hat{N}_{\text{corrected}}^{(k)} \leftarrow |\hat{R}| \odot \exp(i\theta_{\hat{N}_{\text{hist}}^{(k)}}); \quad // \text{ Restore spectrum}$$

$$N^{(k+1)} \leftarrow \frac{1}{\sqrt{HW}} \mathcal{F}^{-1}\{\hat{N}_{\text{corrected}}^{(k)}\} + \mu_{\text{hist}}^{(k)}$$

end

Step 5: Final reconstruction

$$\tilde{I}_{\text{dark}} \leftarrow N^{(K)} + S + \mu^R; \quad // \text{ Restore fixed pattern and mean}$$

return \tilde{I}_{dark}

Table 5: Denoising performance when the system gain g is estimated from either a single noisy image or 16 clean-noisy pairs. Results are reported in PSNR / SSIM.

Dataset	Ratio	16 pairs	1 noisy
SID	$\times 100$	43.72 / 0.961	43.57 / 0.961
	$\times 250$	41.30 / 0.944	41.24 / 0.945
	$\times 300$	37.86 / 0.929	37.77 / 0.929
ELD	$\times 100$	47.14 / 0.986	47.13 / 0.986
	$\times 200$	44.78 / 0.966	44.89 / 0.969